

The Effect on Elastic Modulus of Rigid-Matrix Tubular Composite Braid Radius and Braid Angle Change Under Tensile Loading

Cheequn K. Leung, Garrett W. Melenka, David S Nobes, Jason P Carey

Department of Mechanical Engineering, University of Alberta, Edmonton, Alberta

Abstract (100-150 words)

The objective of this paper is to assess changes in braid radius and braid angle of braided composite tubes under tensile loading using stereomicroscope digital image correlation (DIC) based optical measurement techniques. Using this approach, displacement fields were calculated and three dimensional surfaces were reconstructed. The radius of the tube and the braid angle were determined from the reconstructed surfaces and images. With this initial work showing the effects of tensile loading on the tube radius and braid angle also included development of approaches for deconstructing data. Results highlight that there is ~10% difference between findings for elastic modulus between existing investigation techniques and the methods developed here for rigid-matrix composite braids.

Keywords

Braided Composites; Fiber Reinforced Composites; Experimental Methods; Digital Image Correlation; Elastic Modulus; Braid Angle; Geometry

1. Introduction

Braided composites are used in many industries and their use continues to grow [1] as a result of their capability of providing necessary strength and stiffness. The stiffness of a tubular composite braided structure is geometrically dependent on the radius and wall thickness in addition to its unit cell and material-based elastic modulus [2]. Studies have looked at the relations between wall thickness, braid angle, and braid radius because of their importance in characterizing composite braids as structural components [3], [4]. Thus, knowing the radius and braid angle of a tubular braided composite is critical for stiffness critical applications and composite braid modeling.

A new technique, digital image correlation (DIC), is now being used for textile-based composites to characterize elastic properties and geometries. The technique measures surface deformation by comparing the relative gray scale intensities between a reference and deformed image [5]. The reference and deformed images are divided into evenly spaced subsets forming a grid. Each subset contains variations in gray scale, which are used to match the subset between a reference and deformed image. A correlation algorithm is applied within each subset to find the location of peak correlation between the reference and deformed image. The vector from the center of the subset to the location of peak correlation is the average displacement vector for the subset. The reference and deformed image are cross correlated to give a displacement vector field. The progression from 2D vector fields to the calculation of 3D vector fields requires two cameras. Surfaces are reconstructed by first identifying similar points between stereo image pairs. A stereo cross-correlation algorithm uses the identified points to find the corresponding points between the two images. Mapping functions, which were calculated during calibration, are then used to determine the x , y , and z coordinates of all points that can be used to describe the surface of the geometry.

The mapping functions and the surface are then used to combine the two vector displacement fields from camera 1 and 2 to create a 3D vector field [6].

Studies that apply DIC to textile composites commonly focus on the onset and growth of damage. In some studies, DIC reconstructed surfaces were used as a visualization tool for damage progression of fiber composite pressure vessels [7]. Others have used 3D DIC to reconstruct and measure surfaces of cylinders [8], [9], and a satellite dish [10]. These studies focused mainly on the ability to reconstruct an accurate surface using DIC. A further study, by Luo and Chen [11], measured the curved surface of a cylinder under axial loading. This expanded surface measurements to include deformation.

Many studies have looked at the effect of braid angle on elastic properties of composite braids, both experimentally [4], [12–14] and theoretically [15–19]. A diamond braid preform architecture and a post cure composite braid are shown in Figure 1. A sample-based coordinate system convention is also given in this figure with the x -axis positive to the right, y -axis positive to the top, and the z -axis is positive out of the page. The strength and stiffness of a composite braid can be largely influenced by braid angle [20]. Braids are cross ply composites, where the strand angles are mirrored about the central axial axis of the structure. The braid angle (θ) is defined as the angle of the strands relative to the axial direction of the braid. It is an important geometric factor that greatly affects the mechanical properties of composite braids [17].

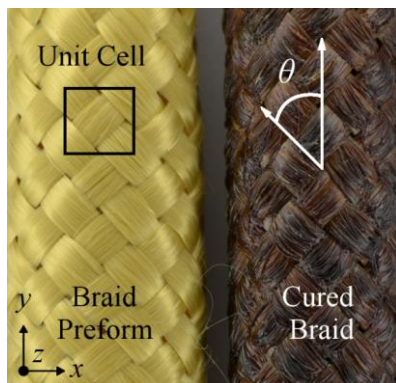


Figure 1 – A braided preform and cured braid with the coordinate system convention.

Xu *et al.* [15] modeled biaxial and triaxial braids of differing textile architectures to predict the material properties with relation to the braid angle. Other studies looked into the effect of fiber architecture on the deformation and elastic moduli of braided composites both experimentally and analytically [1], [12], [14], [16], [20–22]. It was found that for tubular braided composites, as braid angle decreases the longitudinal elastic modulus increases. However, these studies assume that the braid angle remains constant during loading. Studies focusing on the change in braid angle during loading have not been found.

The length, radius and braid angle of a tubular braid preform are all dependent on one another [3], [20]; when a braid preform is loaded in the axial direction the braid lengthens in the axial direction, decreasing the radius and braid angle of the braid. In an epoxy matrix composite braid similar behavior is expected

from the reinforcing fibers; however, it has been assumed in the current literature that the rigid matrix prevents large scale deformations from occurring [17]. If the braid radius experiences changes, the cross sectional area of the sample will also change, altering stress calculations and affecting the accuracy of predictive models [12], [21]. Contrary to all current methods, we propose to ~~determine-investigate~~ the effect of using the instantaneous cross sectional area to calculate stress and elastic properties to provide more accurate experimental data for modeling.

This study aims to investigate the change in outer surface nominal radius, and unit cell braid angle of tubular composite braids. Loading on these tubes under progressively increasing tensile loading will be determined using 3D DIC to determine surface strain and surfaces reconstruction. It further aims to provide insight on the impact of radius and braid angle changes on experimental measurements and elastic moduli prediction models.

2. Methods

Sample Preparation

Tubular diamond braided composites were used in this study follow the procedures of previous work in our research group [21]. The braided sock preforms were produced using a braider (K80-72, Steeger USA, Inman, South Carolina, USA) configured to produce diamond braid patterns. Kevlar fibers (Kevlar 49, 5680 Denier, Dupont, Mississauga, Ontario, Canada) were used as the reinforcement material. The preform was placed over a smooth ~~Polytetrafluoroethylene-polytetrafluoroethylene~~ (PTFE) mandrel with an outer diameter of 11.39 ± 0.03 mm. Fibers were manually impregnated with a thermoset epoxy consisting of an EPON Resin 825 (Resolution Performance Products, Pueblo, CO) and an Ancamine 482 hardener (Air Products and Chemicals, Allentown, PA) mixed at a 100:19 weight ratio. The braids were placed upright in an oven to ensure an even coating and allowed to cure for 2 hours at 110°C [21]. The cured braids were cut to length and bonded to end tabs using the same epoxy resin and curing process as the braid matrices to allow for tensile testing.

A total of 31 braided composite samples were manufactured with the following average standard deviation geometric characteristics: **braid angles of $42.48 \pm 1.96^\circ$** , gauge lengths of 90.82 ± 1.54 mm, wall thicknesses of 1.02 ± 0.05 mm, and outer radii of 6.65 ± 0.06 mm. Gauge length and wall thickness measurements were made using a digital caliper ($0-150$ mm ± 10 μm , Mastercraft, Canadian Tire). Outer radii measurements were made three times on each braid sample using a micrometer (Outside Micrometer $0-25$ mm ± 5 μm , Mitutoyo, Mississauga, Ontario, Canada).

A randomized speckle pattern was applied to the surface of the braids to perform DIC based measurements as detailed in Leung *et al.* [9]. Braids were first painted with a flat black spray paint to reduce lighting reflections, and give a cleaner speckling surface. A fluorescent paint (Createx 5404, Createx Colors, East Granby CT) and reducer (Createx W100 Wicked, Createx Colors, East Granby CT) was used at a 2:1 ratio. The fluorescent speckle pattern was applied using the mixed paint and an airbrush (custom-B micron, Iwata-medea Inc, Portland OR), similarly to Berfield [23]. To excite the fluorescent paint speckles, a 2.64" ring light (Edmund Optics, Barrington, NJ, USA) with a 365nm black-light (Edmund Optics, Barrington, NJ, USA) was used. An example image of the resulting speckle pattern is shown in Figure 2. The image covers approximately 2 unit cells and braids as well as individual fibers can be discerned.

Commented [DSN1]:

Is it important that we document how this angle was measured? We are proposing a new angle measurement approach, so what are we comparing against here?

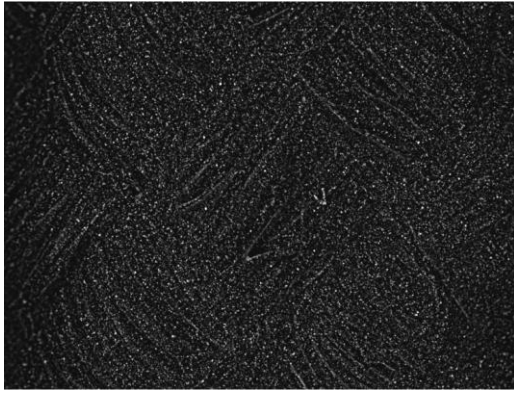


Figure 2 – Images of a sample surfaces with the applied fluorescent speckling pattern. White marks indicate the fluorescent particles applied to the braid surface. Braid fiber tows can also be seen.

Experimental Setup

For this study digital image correlation was used to measure surface deformation and reconstruct the surface of the composite braid samples. The testing equipment and its arrangement used for this study can be seen in Figure 3. The two 1376×1040 pixel, 12bit, charged-couple device (CCD) cameras (LaVision Imager Intense, LaVision GmbH, Gottingen, Germany) used for capturing images were attached to a stereomicroscope (Zeiss Stereo Discovery V8, Carl Zeiss MicroImaging GmbH, Gottingen, Germany). The stereomicroscope was mounted onto a rail extending from the three axis translation stage (LES 5, isel Germany AG, Eichenzell, Germany). The translation stage allowed the camera views to move between multiple regions of interest during a test with a resolution of 1 μ m. A tensile frame (MTS, Eden Prairie, MN USA) was used to load the composite tubular braid samples axially. Load data was obtained from the tensile frame's ± 453.6 kg (± 1000 lb) load cell (661.12B, MTS, Minneapolis, MN, USA), which has an error of 1.5% of the full scale load. Controlling the translation stages and triggering the cameras to capture an image was performed from a control PC. The same optical measurement system was used in a previously published study [9]. The system has a resolution of 1.54 μ m, and in plane and out of plane motion measurement errors of 1.38 \pm 0.54% and 2.14 \pm 0.71% respectively.

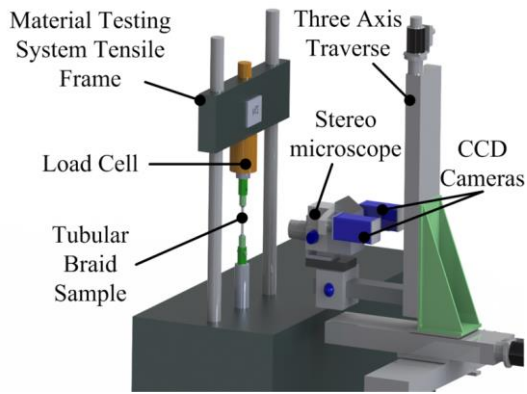


Figure 3 – The experimental setup including the tensile frame and the optical measurement system.

Calibration Procedure

Calibration of the camera system is of great importance when using a multiple cameras for surface measurements [24] as errors in 3D surface reconstruction can stem from calibration and system setup [25]. The intrinsic and extrinsic camera parameters are determined through the calibration process [26]. Lens defects and distortions are corrected through the intrinsic parameters. Relative camera positions and orientations are described through the extrinsic parameters. The calibration process also applies a scale to the images, mapping the images from pixel to physical space. For this study a 2D calibration plate was used for a 3D calibration. The in-plane scales were defined from the 0.5mm dot spacing of the calibration plate. The out-of-plane scale was defined by moving the calibration plate in the out-of-plane (z as defined in Figure 1) direction by known amounts using a micrometer driven stage (MT01 Translation Stage, Thor Labs, Newton NJ, USA). This calibration procedure was validated in a previous study using the same camera system [9].

Post Processing and Surface Reconstruction

A total of 60 stereo image pairs were captured for each sample with 20 stereo image pairs in each image set of the three regions of interest. Starting with a unit cell located at the mid span of the sample (region 1), every other unit cell along the axial direction was chosen. The areas containing the unit cells are defined as Region 1, 2 and 3 as shown in Figure 4. The center of each of these regions of interest is spaced approximately 9mm apart from one another on the sample tubular braids.

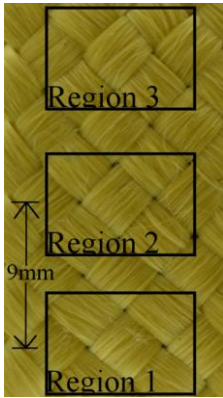


Figure 4 - Location of imaged unit cells relative to one another on a single sample.

Post processing of the image sets was performed using commercial software (DaVis Version 8.0.6 StrainMaster 3D, LaVision GmbH, Gottingen, Germany). A subtract-sliding-minimum filter was applied to all images to increase the contrast in the images. The filter subtracts the local minimum predefined kernel that is applied over the entire image. This removes background intensities while minimal effect of local maxima, the data, giving greater contrast to the speckle pattern. The $\times 1.0$ objective of the stereomicroscope has a shallow focal depth relative to the diameter of the tube. As a result the left and right side of the images were out of focus. These areas in the image were masked out prior to cross-correlating and creating the surface. An example reconstructed composite braid surface is shown in Figure 5. The reconstructed surface has an array size of 900×800 data points. With the stereomicroscope magnification, details of fiber bundles within each strand can be clearly discerned.

Commented [DSN2]:
Arrows on the dimension line in the figure?

Surface Height (mm)

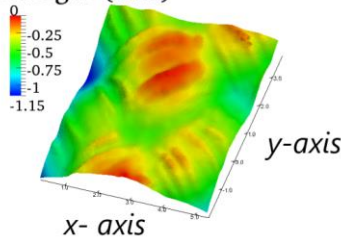


Figure 5 – A surface reconstruction from a stereo image pair. The zero in the scale represents the mid span of the focal depth.

Displacement vector fields that describe the surface motion of the composite braids during testing, as shown in Figure 6, were calculated using multiple passes. A 256×256 pixel size subset was used for the first pass, followed by three passes with a smaller 64×64 pixel subset. All passes used a 75% overlap. The larger subset of the first pass is meant to capture the largest motions observed during the test. The largest motions would occur in the frames that captured sample failure. The smaller subset passes captured

smaller motions observed between most frames and would also give a much denser field of displacement vectors. Strain of the test samples was measured using the DIC calculated displacement fields. The neighboring displacement vectors within the selected area are compared to one another, generating a displacement gradient or strain map.

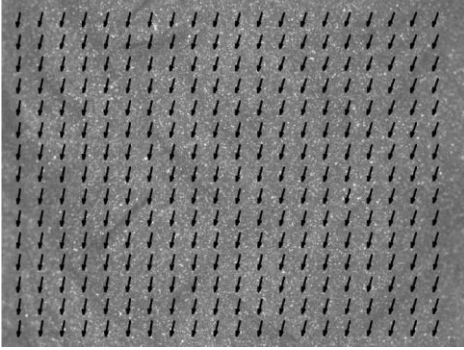


Figure 6- The displacement vector field of a composite braid under loading. The vector density has been reduced to 1 in 8 for clarity.

Braid Radius Measurement

To determine the braid radius, a circle was fitted to the out-of-plane locations of the braid determine from the DIC surface reconstruction. Braid radius was calculated using the 3D displacement vectors from the 3D DIC measurement process and a custom program (The MathWorks, Inc., Matlab, Natick, MA, USA). The fitted circle is created by minimizing the sum of squared radial deviations from all points on the cross section using equations 1 and 2 [27]. The coefficients a , b_1 , b_2 , and c are solved using the coordinates from point 1 and 2, as represented by p_1 and p_2 . $\|b\|$ is the norm of b_1 and b_2 . The radius of the estimated circle, represented by r , can then be found using the coefficients from equation 1.

$$\left(p_1 + \frac{b_1}{2a}\right)^2 + \left(p_2 + \frac{b_2}{2a}\right)^2 = \frac{\|b\|^2}{4a^2} - \frac{c}{a} \quad (1)$$

$$r = \sqrt{\frac{\|b\|^2}{4a^2} - \frac{c}{a}} \quad (2)$$

An example of the estimated circle fitting is shown in Figure 7. The cross section data points taken from the reconstructed surface, shown in blue, form a semicircle along the top. The estimates circle, shown in red, is fit to the data points.

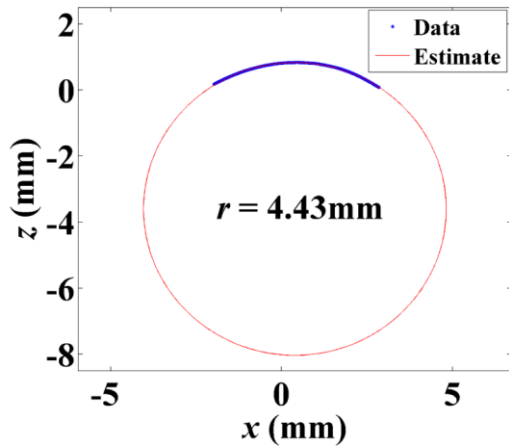


Figure 7 – An example of an estimated circle fit to a series of data points taken from the reconstructed surfaces.

Radii measurements are an average of 60 cross section measurements in the y or axial-direction of the tube with equal spacing between each measurement, over the unit cell. The unit cell span where the cross sections were taken is shown in Figure 8, between the upper and lower limits. The line at the selected point is the reference cross section for the measurement. Twenty nine measurements are made above the reference cross section and the remaining thirty are made below. This averaging approach was used because of the undulating surface profile, as shown in Figure 5 of the tube.

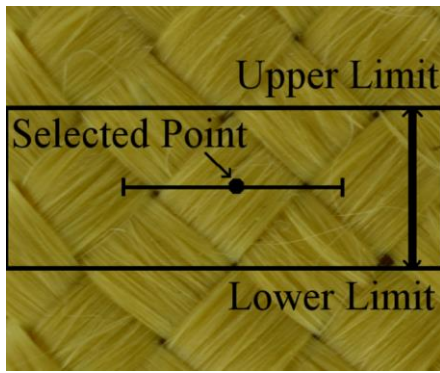


Figure 8 – The span of the central unit cell, around the selected point, where radii measurements were taken.

Braid Angle Measurement

Braid angle measurements were made on the captured images during testing. The braid angle was measured from the unit cell centered in the field-of-view. Points selected from the unit cell were selected as shown in Figure 9. The top corner of the central unit cell and the top corner of the unit cell beneath the central unit are connected to create the axial axis line. The left and right points are each connected with the top corner of the unit cell beneath the central unit to give a bottom left and bottom right line,

respectively. All three of the lines are represented by vectors. The bottom left and bottom right lines are both represented by vector u , while the axial axis line is represented by vector v . The magnitudes of the vectors u and v are given by $\|u\|$ and $\|v\|$. Braid angles were calculated using equation 3, which gives the angle (θ) between two vectors.

$$\cos(\theta) = \frac{u \bullet v}{\|u\| \|v\|} \quad (3)$$

The negative braid angle is found using the vectors representing the bottom left and axial line. The positive braid angle is found using the vectors representing the bottom right and axial line. The magnitude of the two braid angles are averaged to give the braid angle measurement for that frame. For each subsequent frame the selected points at the four corners are tracked using the displacement vector fields. At each frame the vectors of each line are recalculated as is the braid angle.

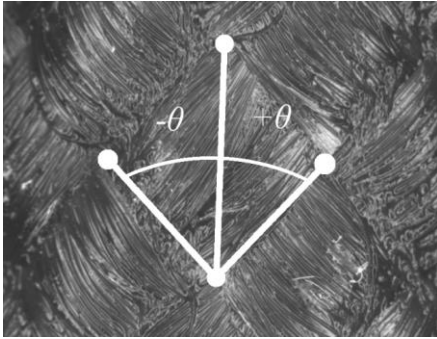


Figure 9 – A braid angle measurement diagram showing the four selected points, the lines formed when the points are connected, and the positive and negative braid angle.

To determine the consistency of chosen points for the braid angle measurement procedure a repeatability test was performed. The initial braid angle of a single sample was measured ten times from the same image using the braid angle measurement procedure described above. The measurements of this single sample gave an average braid angle and standard deviation of $45.49 \pm 0.54^\circ$.

Tensile Test Procedure

A braid sample was secured in the grips of the tensile frame. The cameras were centered and focused in Region 1 where the coordinates of the translation stage are recorded. The cameras were then traversed upwards to unit cells in Region 2 and 3 to ensure that the cameras are properly centered and focused in these regions as well. Before the first test was run the sample was removed from the tensile frame to perform the camera calibration procedure at each of the three regions. The sample was then reinserted into the tensile frame. An initial stereo image pair was captured in Region 1 before traversing the cameras to Region 2 and 3. Scanning through the three regions once captures one stereo image pair of each region for a total of six images per scan. Two scans are completed without applied loading to ensure that the initial unloaded state of the sample is captured. After two scans, the tensile frame is started and stroke controlled with a pull rate of $7.6 \mu\text{m/s}$ for a total stroke of 2.65mm. The stroke is continuous throughout

the test. During loading the cameras scan over the three regions a total of twenty (20) times creating complete image sets of 20 stereo image pairs for each region. A total of sixty (60) stereo image pairs are captured for each test sample. At this point the image capturing and tensile frame loading is stopped. This process was repeated for each sample.

Data between the regions is collected at different time intervals. The data points cannot be compared directly. Only the overall stress strain responses between the regions could be compared. At maximum stroke the samples are expected to reach a strain of 2.9%. This level of strain is beyond the expected failure point, which is approximately 1.5% strain for similar braid angles [17]. The total stroke was chosen to allow for braid radius change to be evaluated through to failure. When the matrix has cracked and can no longer maintain a rigid tubular shape the braid is considered to have failed.

3. Results

Within each test, a braided composite sample is loaded uniaxially from an unloaded state to failure. The stereomicroscope cameras captured this motion with the left and right cameras and 3D surfaces were reconstructed. The progression of one test sample from an unloaded state to failure is shown in Figure 10, as captured by the cameras and reconstructed surfaces. The colour map in the figure is scaled to a zero position of the 3D reconstructions that has been identified as the highest point (z direction) of the surface. Strain measurements were made in the y -direction as an average of the strain field over the sample surface. The sample begins in an unloaded state as shown in Figure 10(a). The sample is loaded, reaching strains of 0.69% in Figure 10(b) and 1.87% in Figure 10(c). Cracks begin to form in the matrix of the composite, and can be seen as a ridge at the bottom right edge of the central unit cell in the surface reconstruction of Figure 10(d). At complete failure, in Figure 10(e), the matrix cracking has progressed extensively through the structure. The DIC system calculated average strains of 4.20% and 8.82% in Figure 10(d) and (e), respectively. However, local strains could be inaccurate due to the matrix cracking that allows separated pieces of the speckled surface to shift apart. As we progress from Figure 10(a) to Figure 10(e) the red and yellow regions account for more and more of the unit cell surface. This indicates a reduction in the relative height difference between high and low points on the braid.

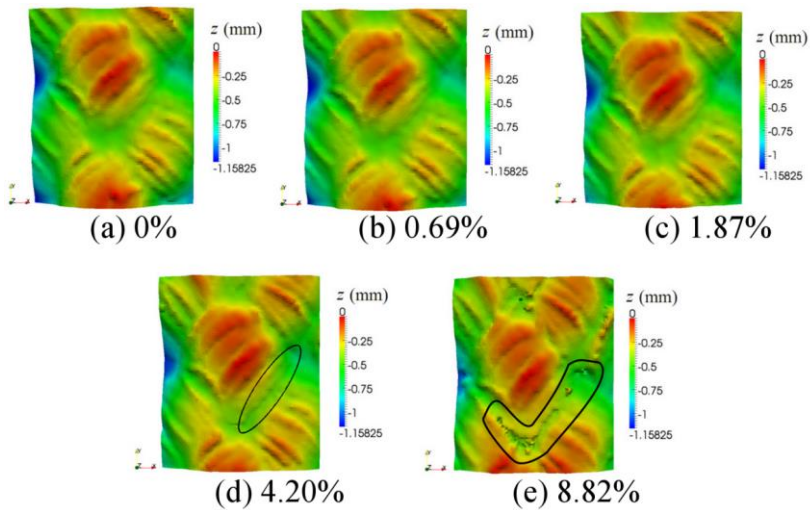


Figure 10 – Three dimensional surfaces of a test sample as it progresses from (a) an unloaded state to (e) failure. The colour scale is relative to the highest point on the surface. Cracks are outlined in (d) and (e).

Before failure, samples reached an average strain of $1.64 \pm 0.67\%$ in region 1. This is the average and standard deviation of the y -direction strains reached by all samples at the image frames before failure. The standard deviation is considerable and may be attributed to the factors outlined below. Displacements and strains were calculated from the images. However, matrix cracking was not always present at the location where images were captured. Images with large crack formation may have experienced local stress and strain concentrations, and could result in larger calculated strains compared to image sets with little or no cracking. The manual application of epoxy matrix resin to the fiber preform can produce in an imperfect matrix, resulting in local stress and strain concentrations. Finally, the braids may experience combined loading due to misalignments between the end tabs.

Braid Radius Change

The radius measurements in Region 1 for all samples are given in Figure 11(a). Data after failure sample is removed. The average measured radius of the unloaded samples is 5.36 ± 0.40 mm. Failures occur as early as frame 14, with the majority failing at frame 18. Sample measurements made after sample failure are removed in all further plots, unless otherwise specified.

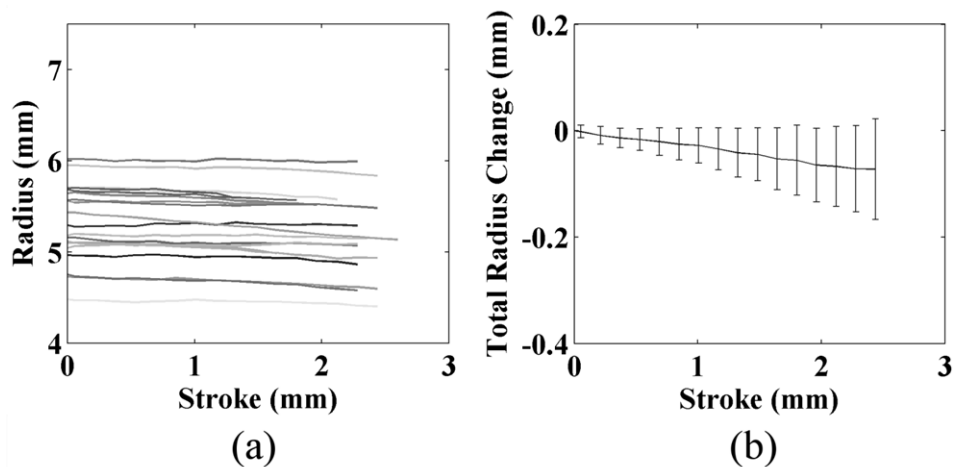


Figure 11 – (a) The radius measurements in region 1 of all samples, with measurements after sample failure removed and (b) the total radius change as a function of stroke.

The difference in radius measurement between the initial frame (frame 1) and a later frame gives the change in radius of a sample resulting from loading. The total radius change at each frame was averaged over all samples and is shown in Figure 11(b). At the final frame the average total radius change of all samples is -0.072 ± 0.095 mm. The standard deviations of the total radius change averages increase throughout the test, maintaining a standard deviation of a similar magnitude to the average change.

Braid Angle Change

Braid angle measurements for all samples, with data after failure removed, are shown in Figure 12(a). The average initial braid angle of the cured samples is $42.48 \pm 1.96^\circ$. The initial braid angle can range from 39° – 46° as a result of the hand resin impregnation technique used to form the composite braid samples. Similar braid angle variations of $44.19 \pm 1.63^\circ$ and $50.56 \pm 2.16^\circ$ for composite braided tubes samples were found in a study by Ayranci *et al.* [21]; samples of which were also manufactured by hand and used Kevlar fibers.

Commented [DSN3]:

How does this affect the angle so much? Is there solid evidence to support this?
I would imagine that the winding technique would be the major impact.

Commented [CL4]: I have no test data to support this. We need to do a test to see how much the braid angle varies before and after hand resin impregnation. Otherwise we may have to remove these comments for this journal?

Commented [JPR5]: This is a well known fact of any hand impregnation technique.

Formatted: Font: Italic

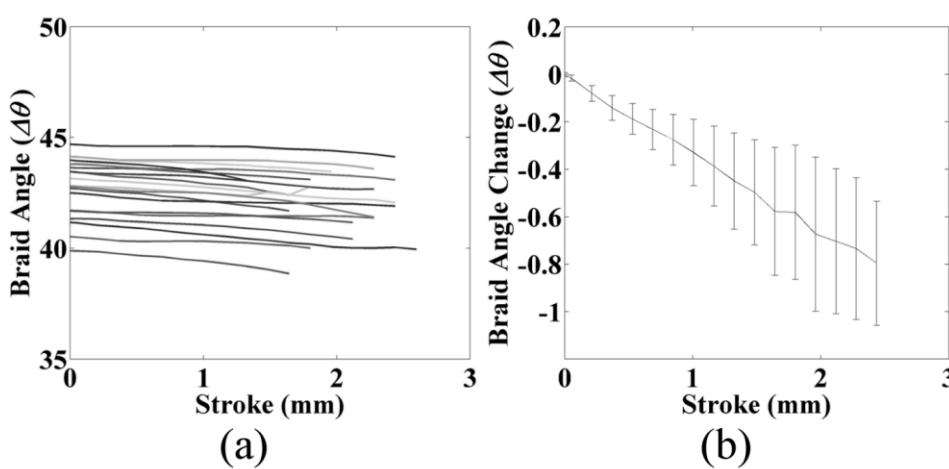


Figure 12 – (a) Braid angles of all samples in Region 1 as a function of stroke, with data after failure removed and (b) the average total braid angle change of all samples as a function of stroke.

Sample preforms were manufactured with an expected braid angle of 45° . The initial braid angles of the cured samples were found to be $42.48 \pm 1.96^\circ$. This discrepancy can be attributed to the hand manufacturing process of samples. The preforms are braided on a mandrel with a smaller diameter than the final product. The first change in braid angle occurs when the preforms are placed onto mandrels with the final product diameter. This increase of inner diameter for the braid preforms alters the braid angle. The epoxy is then massaged into the braids by hand, further shifting the braid angle; all efforts are made to ensure the braid angle is set as consistently as possible.

The braid angle at the center of the braid (Region 1) can be seen decreasing in Figure 12(b). By the last frame the braid angle has changed by $-0.80 \pm 0.26^\circ$. The standard deviations increase with each subsequent frame until frame 15, where it reaches its maximum of $\pm 0.33^\circ$. The standard deviation then decreases for the remaining frames, as samples fail and are removed from the pool of averaged samples.

Three Region Comparisons

Images were captured of the unit cells at the three designated regions for each test sample. The measurements in each region are compared to determine if similar behaviors are being seen across the braid structure. The average total radius change experienced before sample failure in regions 1, 2, and 3 are -0.077 ± 0.080 mm, -0.118 ± 0.083 mm, and -0.113 ± 0.076 mm, respectively. All regions experienced a decrease in radius on the scale of $100 \mu\text{m}$. The standard deviations are all within similar ranges. The average braid angle changes reached before sample failure for regions 1, 2, and 3 are $-0.80 \pm 0.26^\circ$, $-0.81 \pm 0.33^\circ$, and $-0.79 \pm 0.37^\circ$, respectively.

4. Discussion

Braid Radius Change Effects

Commented [DSN6]: Wrong symbol for theta!
In 11(b) it should be something like $\Delta\theta$!

Commented [JPR7]: I think the delta theta thing was not changed in fig b

Commented [DSN8]:
Again, what evidence is there for this?

Commented [JPR9]: Again, very old citations may be found. A study could be useful in Garrett's thesis. For this paper, citing cagri I think is sufficient

Commented [GM10]: This might be an interesting study. Measure braid angle on the original mandrel, measure braid angle on the curing mandrel before epoxy and then measure braid angle after hand massaging the epoxy to see how braid angle is changed.

Commented [CL11]: We will need a study to provide any solid evidence of this. Otherwise it is speculation. Should we remove it from the discussion?

The radii measurements contain large standard deviations. Possible reasons for the inaccuracy include a shallow focal depth, and rough uneven sample surfaces. The surface beyond the focal depth is out of focus and cannot be accurately reconstructed, as shown in Figure 13, and is removed. The area of surface reconstructed is reduced, limiting the amount of surface available for the circle fitting process.

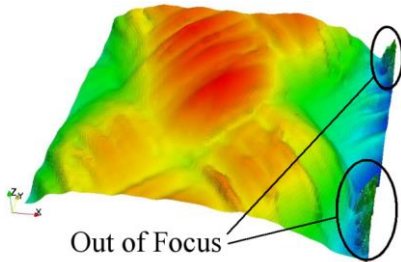


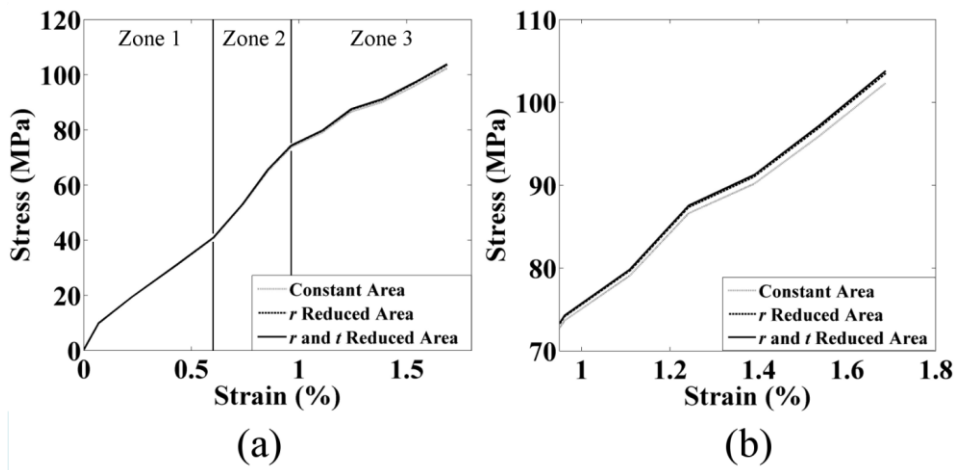
Figure 13 – A braided composite surface reconstruction including out of focus regions that are circled.

The radii of the braids were measured using a micrometer prior to testing. This measurement technique is also affected by the surface roughness. The micrometer arms contact surface is a circle with a 5mm diameter. This large surface causes the arm to contact and stop at the peaks of the unit cells. As a result, the micrometer measurements are affected by the surface roughness and measure surface radius that is weighted by the maximum surface heights. The 3D DIC surface reconstruction measurements fit a circle to the average of the surface. DIC radii measurements, which averaged sixty measurements across a single unit cell, minimize the impact of surface roughness. Radii measurements using DIC should give an outer radius measurement that averages the peaks and valleys across, and thus should be smaller than the micrometer measurements. The average unloaded sample radii measured from Region 1 using DIC is $5.36 \pm 0.40 \text{ mm}$, which is 19.4% smaller than the micrometer measurement of $6.65 \pm 0.06 \text{ mm}$. The wall thickness of the braids is $1.02 \pm 0.05 \text{ mm}$ which suggest a strand thickness of 0.51mm. The difference between surface heights at the peak and valley locations is 0.51mm. However, the inside surface of the braids contacted the mandrel during curing and are smooth. Thus, the difference in surface height is likely more than half the wall thickness. The DIC measurement method considers surface features and measures the average radius of these features, while the micrometer measures the radius given by the peak surface features. Furthermore, the DIC measurements were heavily influenced by surface features, particularly across the center of the unit cell. The circle fit equation estimated circle fit more closely to the unit cell peak surface feature rather than the overall surface features due to a limited fitting surface. This could explain the difference between the DIC averages and micrometer measurements. Furthermore, it could indicate post curing residual stresses that lead to a contraction after mandrel removal.

An average radii change of approximately -0.1mm was measured from the DIC method. Calculating from the averaged values of the braid samples, the average undeformed cross sectional area of the braids is 39.41 mm^2 . If the thickness is held constant but the outer radius has decreased from loading the deformed cross section is 38.77 mm^2 . The total difference in cross sectional area after the radius change is -1.7% over an axial strain range of 1.84%. This would lead to an increase in calculated instantaneous stress.

Sample thickness also affects the cross sectional area but cannot be measured with the current images captured. Biaxial braided composites are similar to angle-ply laminates [$\pm\theta$], which can be described

using classical laminate theory (CLT) [28]. Using CLT to calculate the through thickness Poisson ratio of 0.32 for the composite, the thickness change resulting from loading was estimated as $-5\mu\text{m}$. The combined radius and thickness change results in a 2.12% decrease in cross sectional area before sample failure. The effect of cross sectional area change due to radius and thickness change can be found in Figure 14. In the plot the reduction in area was applied linearly such that the total cross sectional area reduction is reached at the end. The stress strain response has three distinct zones with linear slopes between 0-0.6% strain (Zone 1), 0.6-0.96% strain (Zone 2), and 0.96%-1.69% strain (Zone 3). The tangent moduli for the constant cross sectional area plot are 5.48GPa, 9.16GPa, and 3.95GPa in Zones 1, 2, and 3 respectively, with an average modulus of 6.06GPa. The radius and thickness reduced cross sectional area plot tangent moduli are ~~5.52GPa~~ 5.2GPa, 9.27GPa, and 4.07GPa in zones 1, 2, and 3 respectively, with an average modulus of 6.15GPa. Clearly, there is a non-linear stress-strain behavior that is an influence of geometry.



Commented [JPR12]: The different lines are much harder to see now. Could we have a part b of this image that shows a close up of zone three from 70 MPA to 110?

Figure 14 – (a) A stress strain plot showing the effect of reduced cross sectional area from changing radius and thickness. Lines are for visual purposes only. Zone 1 0-0.6% Strain. Zone 2 0.6-0.96% strain. Zone 3 0.96-1.69% strain. (b) A close up of zone 3.

A study by Carey *et al.* [16] loaded braided composite tubes uniaxially and compared the experimentally determined longitudinal elastic modulus as a function of braid angle to a prediction model. The expected longitudinal elastic modulus from the proposed model overestimated the experimentally determined values. In this study the cross sectional area was considered constant, thus engineering stress was used. A longitudinal elastic modulus of 6.25GPa was experimentally determined for samples with braid angles of 42.5° . A reduction in cross sectional area of 2.12% would increase the calculated longitudinal elastic modulus to 6.38GPa. The proposed model predicts a longitudinal elastic modulus of approximately 7GPa for a braid angle of 42.5° . The reduction in cross sectional area due to radius and thickness change does not fully bridge the gap between experimental and predicted values.

Braid Angle Change Effects

Over the duration of the test, the average braid angle decreased by 0.80° , from an initial angle of 42.7° to a final angle of 41.9° . To determine the effect of braid angle change on composite braid properties, studies that measured material properties as a function of braid angle were examined. Results from a tubular composite braid model for rigid epoxies, adapted from Carey *et al.* [16], predicting the longitudinal elastic modulus can be seen in Figure 15. From the modulus curve, it can be seen that a braid angle change of less than 1° within the range of 50° - 60° does not drastically affect the longitudinal modulus of the braid. However, between the range of 30° - 45° the longitudinal modulus is extremely sensitive to a change in braid angle. From 30° - 35° the modulus decreases by 25.2% from 14.3GPa to 10.7GPa. A braid angle change of 1° from 35° to 34° would increase the modulus from 10.7GPa to 11.42GPa. This is a 7% change and can greatly affect how the composite braid behaves. A change of this magnitude could greatly affect the design of any composite braids used in stiffness critical applications. The discrepancy between the experimental and model longitudinal elastic modulus values are near 7%. The changing braid angle and cross sectional area may account for this discrepancy.

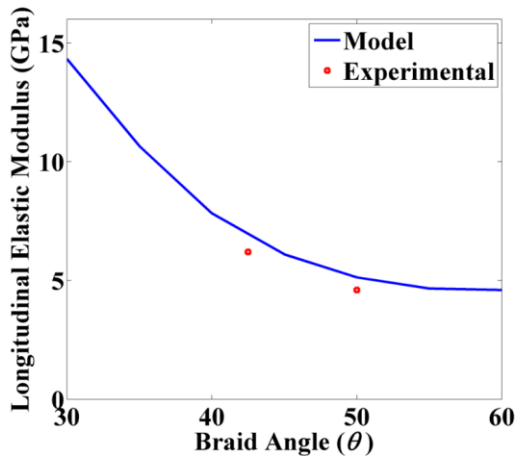


Figure 15 - Model predictions and experimental values of longitudinal moduli for Kevlar 49/epoxy closed mesh braids as a function of braid angle recreated from a study by Carey *et al.* [16]

Due to decreasing braid radius and wall thickness we expect a total cross sectional area decrease of - 2.12% before sample failure. If strain measurements remain the same the stress would increase by 2.12%, and in turn so would the longitudinal elastic modulus. The measured stress directly influences the calculation of elastic and shear moduli. This is compounded with the change in braid angle. The braid angle decreases with axial tension which further increases the longitudinal moduli. When the angle change is compared with the model in Figure 15, an increase in modulus of $\sim 7\%$ is expected. If the effects of braid radius and braid angle change are combined, the longitudinal elastic modulus of a braid may change by 9.12% before failure occurs. This change in modulus could be detrimental to the performance of composite braids and must be considered in models and when designing composite braid structures for stiffness critical applications. The effect could be further amplified if elastomeric polymers were used for the composite matrix.

The matrix constitutes approximately 40% of a composite's volume and can largely influence the longitudinal elastic modulus [16]. The resin used in the manufacturing of the braided composite samples for this study gave a rigid matrix. However, braided composites can also be manufactured with an elastomeric matrix. The main difference is that elastomers have a low modulus of elasticity compared to rigid epoxies [16]. Thus, we would expect an elastomeric polymer matrix composite to reach higher strains resulting in further reduction of both radius and wall thickness.

5. Conclusions

The radius braid angle change of composite tubular braids under axial loading was successfully investigated using imaging technology. The initiation and propagation of matrix cracking could be seen occurring in the captured images. Both radius and braid angle measurements were consistent when comparing across all three regions, suggesting that evaluating one unit cell in the gauge length is sufficient to describe radius change throughout the braid.

The radius change of tubular composite braids under axial loading was examined using 3D DIC surface reconstructions. The results from this test suggest that the composite braids experience a small decrease in radius on the order of 100 μ m. This radius change would decrease the cross sectional area, increasing the stress and affecting the calculated moduli. Braid angle changes as a function of tensile loading was measured for the first time. An average braid angle change of $-0.80 \pm 0.26^\circ$ was found at the center of the braid. A braid angle change of one degree can largely affect elastic moduli, depending on the initial braid angle, and should be considered in future design or models. The difference between modeled and experimental modulus values can potentially be attributed to the change in braid angle as well as a decrease in cross sectional area.

Together, we found that radius and braid angle changes could affect elastic modulus results by nearly 10%. The decrease of radius and change in braid angle and their effects on stress and moduli calculation would be further amplified for elastomeric resin based composites and will be the focus of future work.

6. Acknowledgements

The authors acknowledge funding support for this research from the Alberta Ingenuity Fund, the Natural Sciences and Research Council (NSERC) of Canada and the Canadian Foundation for Innovation.

References

- [1] J. Carey, M. Munro, and A. Fahim, "Longitudinal Elastic Modulus Prediction of a 2-D Braided Fiber Composite," *Journal of Reinforced Plastics and Composites*, 2011.
- [2] J. Carey, A. Fahim, and M. Munro, "Design of Braided Composite Cardiovascular Catheters Based on Required Axial, Flexural, and Torsional Rigidities," *Journal of biomedical materials research. Part B, Applied biomaterials*, vol. 70, no. 1, pp. 73-81, Jul. 2004.

- [3] H. Ghiasi, L. Lessard, D. Pasini, and M. Thouin, "Optimum Structural and Manufacturing Design of a Braided Hollow Composite Part," *Applied Composite Materials*, vol. 17, no. 2, pp. 159-173, Oct. 2009.
- [4] P. Potluri, A. Manan, M. Francke, and R. Day, "Flexural and Torsional Behaviour of Biaxial and Triaxial Braided Composite Structures," *Composite Structures*, vol. 75, no. 1-4, pp. 377-386, Sep. 2006.
- [5] B. Pan, K. Qian, H. Xie, and A. Asundi, "Two-Dimensional Digital Image Correlation for In-Plane Displacement and Strain Measurement: A Review," *Measurement Science and Technology*, vol. 20, no. 6, p. 062001, Jun. 2009.
- [6] LaVision GmbH, "DaVis 72 Product Manual - StrainMaster 3D - Getting Started." Gottingen, Germany, p. 92, 2007.
- [7] L. B. Meng, G. C. Jin, X. F. Yao, and H. Y. Yeh, "3D Full-Field Deformation Monitoring of Fiber Composite Pressure Vessel Using 3D Digital Speckle Correlation Method," *Polymer Testing*, vol. 25, pp. 42-48, 2006.
- [8] P. F. Luo, "Measurement of Curved Surface by Stereo Vision and Error Analysis," *Optics and Lasers in Engineering*, vol. 30, no. 6, pp. 471-486, Dec. 1998.
- [9] C. K. Leung, G. Melenka, D. S. Nobes, and J. P. Carey, "Validation of DIC as an Effective Tool for Composite Tubular Braid Characterization," *CSME International Congress 2012*, pp. 1-6, 2012.
- [10] B. Pan, "Accurate Measurement of Satellite Antenna Surface Using 3D Digital Image Correlation Technique," *Strain*, vol. 40, no. 2, pp. 393-200, Apr. 2009.
- [11] P. F. Luo and J. N. Chen, "Measurement of Curved-Surface Deformation in Cylindrical Coordinates," *Experimental Mechanics*, vol. 1, no. 3, pp. 133-350, Dec. 2000.
- [12] C. Ayranci, D. Romanyk, and J. P. Carey, "Elastic Properties of Large-Open-Mesh 2D Braided Composites: Model Predictions and Initial Experimental Findings," *Polymer Composites*, 2010.
- [13] A. Harte, "Deformation and Dailure Mechanisms of Braided Composite Tubes in Compression and Torsion," *Acta Materialia*, vol. 48, no. 6, pp. 1259-1271, Apr. 2000.
- [14] R. A. Naik, P. G. Ifju, and J. E. Masters, "Effect of Fiber Architecture Parameters," *Journal of Composite Materials*, vol. 28, no. 7, pp. 656-681, 1994.
- [15] L. Xu, S. J. Kim, C.-H. Ong, and S. K. Ha, "Prediction of Material Properties of Biaxial and Triaxial Braided Textile Composites," *Journal of Composite Materials*, no. Jan, pp. 1-16, 2012.
- [16] J. Carey, A. Fahim, and M. Munro, "Predicting Elastic Constants of 2D-Braided Fiber Rigid and Elastomeric-Polymeric Matrix Composites," *Journal of Reinforced Plastics and Composites*, vol. 23, no. 17, pp. 1845-1857, Nov. 2004.

- [17] A. Harte, "On The Mechanics of Braided Composites in Tension," *European Journal of Mechanics - A/Solids*, vol. 19, no. 2, pp. 259-275, Mar. 2000.
- [18] Z. Huang, "The Mechanical Properties of Composites Reinforced With Woven and Braided Fabrics," *Composites Science and Technology*, vol. 60, pp. 479-498, 2000.
- [19] M. M. Shokrieh and M. S. Mazloomi, "An Analytical Method For Calculating Stiffness of Two-Dimensional Tri-Axial Braided Composites," *Composite Structures*, vol. 92, no. 12, pp. 2901-2905, Nov. 2010.
- [20] C. Ayranci and J. Carey, "2D Braided Composites: A Review for Stiffness Critical Applications," *Composite Structures*, vol. 85, no. 1, pp. 43-58, Sep. 2008.
- [21] C. Ayranci and J. P. Carey, "Experimental Validation of a Regression-Based Predictive Model for Elastic Constants of Open Mesh Tubular Diamond-Braid Composites," *Polymer Composites*, 2011.
- [22] A. Ohtani and A. Nakai, "Effect of Internal Structure on Mechanical Properties of Braided Composite Tubes," *16th International Conference on Composite Materials*, pp. 1-5, 2007.
- [23] T. A. Berfield, J. K. Patel, R. G. Shimmin, P. V. Braun, J. Lambros, and N. R. Sottos, "Micro and Nanoscale Deformation Measurement of Surface and Internal Planes via Digital Image Correlation," *Experimental Mechanics*, vol. 47, no. 1, pp. 51-62, Jan. 2007.
- [24] W. Sharpe and W. Sharpe Jr., *Springer Handbook of Experimental Solid Mechanics*. Berlin: Springer, 2008, p. 1098.
- [25] G. Besnard, B. Etchessahar, J.-M. Lagrange, C. Voltz, F. Hild, and S. Roux, "Metrology and Detonics: Analysis of Necking," *Proceedings of SPIE*, vol. 7126, p. 71261N-71261N-12, 2008.
- [26] R. Y. Tsai, "A Versatile Camera Calibration Technique for High-Accuracy 3D Machine Vision Metrology Using Off-the-shelf TV Cameras and Lenses," *Journal of Robotics and Automation*, no. 4, 1987.
- [27] G. H. Golub and R. Strebler, "Least-Squares Fitting of Circles and Ellipses," *BIT*, vol. 34, pp. 558-578, 1994.
- [28] J. Tate, A. Kelkar, and J. Whitcomb, "Effect of Braid Angle on Fatigue Performance of Biaxial Braided Composites," *International Journal of Fatigue*, vol. 28, no. 10, pp. 1239-1247, Oct. 2006.